Contents of this file

- Text S1–S4
- Figures S1–S8
- Table S1

Text S1: Airborne radar data acquisition and processing

This study utilised four airborne radio-echo sounding (RES) surveys:

- AGAP (Antarctica's Gamburtsev Province) 2007/08 (Bell et al., 2011; Ferraccioli et al., 2011)
- PolarGAP 2015/16 (Paxman et al., 2019; Winter et al., 2018)
- Operation IceBridge 2010, 2014, 2016, 2017, and 2018 (MacGregor et al., 2021)
- COLDEX (Centre for Oldest Ice Exploration) 2022/23 and 2023/24 (Young et al., 2025)

British Antarctic Survey RES data (AGAP and PolarGAP) were collected using the 150 MHz Polarimetric radar Airborne Science Instrument (PASIN-1) radar echo sounding system. The AGAP survey utilised the Lamont-Doherty Earth Observatory radar system (also 150 MHz) in tandem with PASIN-1. Operation IceBridge data were collected using the 165–215 MHz Multichannel Coherent Radar Depth Sounder (MCoRDS) system, with the exception of the 2010 season, which used an earlier version of MCoRDS with a centre frequency of 189–199 MHz. The radar instrument used for the COLDEX surveys was the 60 MHz Multifrequency Airborne Radar-sounder for Full-phase Assessment (MARFA) radar system. All radar data were processed using 2D synthetic aperture radar (SAR) focussing.

Positional data (latitude, longitude, and height referenced to the WGS84 ellipsoid) were recorded using dual-frequency GPS with an absolute accuracy of <1 m. Ice thickness was determined by calculating the two-way travel time of radar reflections at the ice surface and bed interfaces. The surface and bed reflectors were picked automatically and manually corrected if necessary. Travel times were converted to depth assuming a uniform electromagnetic wave speed in ice of 0.168–0.169 m/ns (the exact value used was dependent on the survey), with the AGAP and PolarGAP surveys applying an additional 10 m correction for the firn layer. Ice thickness was calculated as the vertical distance between the picked surface and bed. Bed elevation (relative to the WGS84 ellipsoid) was computed by subtracting the ice thickness from the surface elevation (as measured by the survey).

Text S2: Trunk valley and tributary collinearisation

In a steady-state fluvial network, the trunk valley and tributaries should be collinear in χ-elevation space and this can be used to independently constrain the appropriate concavity index (θ) (Goren et al., 2014; Hergarten et al., 2016; Mudd et al., 2014; Perron and Royden, 2013). This method is distinct from constraining θ by determining the maximum value of the correlation coefficient (R) for a linear least-squares regression through all points in the network without considering the interrelationship between tributaries and the trunk valley. We used two metrics to evaluate trunk-tributary collinearity and constrain the best-fitting θ.

First, we calculated the maximum likelihood estimator (MLE) based on the residuals between the elevation of all tributary nodes and the linear regression through the trunk valley in χ-elevation space (Mudd et al., 2018):

$$MLE = \prod_{i=1}^{N} \exp\left[-\frac{r_i^2}{2\sigma^2}\right] \quad (S1)$$

where N is the number of tributary nodes, r_i is the residual between the elevation of tributary node i and the linear regression of elevation on the trunk valley at the corresponding value of χ, and σ is a scaling factor. The residuals will be a function of θ and smaller residuals (i.e., better collinearisation) will yield MLE values closer to 1. However, because the MLE is a product of negative exponentials, its value will decrease as N increases. This means in large datasets MLE values will tend towards zero, even for small residuals, yielding spurious results. To counter this effect, we can increase σ until all θ values return non-zero MLE values, allowing the best-fitting θ (that yields the highest MLE) to be identified. Beyond this point, the best-fitting θ is invariant with increasing σ, so the value of σ is irrelevant provided it is sufficiently high to prevent MLE values of zero. As a result, a large value of σ (>1000) is recommended (Mudd et al., 2018). We found that σ = 6000 ensured all MLE values were above zero, allowing us to constrain the concavity index (Fig. S3).

Second, we calculated a disorder statistic that quantifies the differences in χ-elevation patterns between tributaries and the trunk valley (Goren et al., 2014; Hergarten et al., 2016). This metric is calculated by sorting all χ-elevation pairs in the network by increasing elevation. We then computed the disorder metric as (Hergarten et al., 2016):

$$D = \frac{1}{\chi_{max}}\left(\sum_{i=1}^{N}\left|\chi_{s,i+1} - \chi_{s,i}\right| - \chi_{max}\right) \quad (S2)$$

where $\chi_{s,i}$ represents the i^{th} χ co-ordinate along the network that is sorted by elevation. Since the sum in Eq. (S2) scales with absolute values of χ (and therefore θ), it is adjusted by the maximum value of χ in the network to ensure the disorder metric does not scale with θ. The disorder metric will be minimised if all the χ-elevation co-ordinates in the network are related monotonically, as will be the case if the trunk and tributary channels are perfectly collinear. The minimum D value therefore corresponds to the best-fitting concavity index (Fig. S3).

Text S3: Knickpoints and base-level change

The two knickpoints in segment 1 of the basin 10 longitudinal profile have higher slopes than the regional trend of the channel profile (Fig. S5). In longitudinal profiles, such knickpoints may be transient features propagating upstream, indicative of the profile being in a disequilibrated state of adjustment following one or more episodes of base-level fall (Lague, 2014). We therefore used the stream power incision model to explore this possibility. We updated the original uplift history (where $U(t)$ is constant) to include two pulses of increased uplift rate (i.e., base-level fall) at the end of the model run. The amplitude of

the base-level fall was constrained by the 'relief' of the two knickpoints (210 m for the upper knickpoint and 260 m for the lower knickpoint).

We found that this revised uplift history produced a good agreement with the observed longitudinal profile within segment 1 (Fig. S5a). Assuming base level is situated at the start of the profile (~200 m above sea level), the time taken for the lower and upper knickpoints to propagate from base level to their observed positions was calculated (according to Eq. 13 in the main manuscript) as 0.27–2.7 Myr and 0.84–8.4 Myr, respectively (Fig. S5b). These ranges reflect the range of tested K values corresponding to E = 10–100 m/Myr, with θ = 0.60 and n = 1. If θ is changed to 0.50 (the lowest value recovered from the GSM), the response times of the two knickpoints increase to 0.45–4.5 Myr and 1.3–13 Myr, respectively (Fig. S5b). If n is also allowed to vary between 0.8 and 1.2, the ranges of response times for the upper and lower knickpoints widen to 0.18–6.3 Myr and 0.55–18 Myr, respectively.

Text S4: Flexural modelling

We used 1D flexural modelling to simulate the observed topography of the Recovery Subglacial Highlands. First, the observed bed elevations were adjusted to account for the isostatic response to the unloading of the Antarctic Ice Sheet (Paxman et al., 2022). We then calculated the flexural effects of two processes likely to have driven mountain-range uplift.

First, slip on a normal fault causes unloading of the footwall block by removal of the hanging-wall. The footwall block is therefore flexurally uplifted. Concomitant replacement of footwall crustal rock by the mantle causes isostatic subsidence of the hanging-wall block. Long-term normal fault displacement may therefore be modelled as the flexural isostatic adjustment to the rigid uplift/subsidence of the footwall/hanging-wall blocks, assuming that the lithosphere retains a finite flexural rigidity during extension (Weissel and Karner, 1989).

We calculated the unload geometry assuming a single, purely normal fault with a typical dip of 60° and a given faulted layer thickness (h_0). This allowed us to determine the effective unloading experienced by the footwall block due to downward displacement of the hanging-wall block via slip on the fault (Watts, 2023). Having estimated the geometry of the mechanical unload ($h(x)$; Fig. S7), we calculated the induced flexure ($w(x)$) using the one-dimensional flexure equation for a thin elastic plate overlying an inviscid mantle, which is given by (Watts, 2023):

$$\frac{\partial^2}{\partial x^2}\left[D\frac{\partial^2 w}{\partial x^2}\right] + \left(\rho_{mantle} - \rho_{infill}\right)gw(x) = \left(\rho_{load} - \rho_{displace}\right)gh(x) \qquad (S3)$$

where

$$D = \frac{ET_e^3}{12(1-\upsilon^2)} \quad (S4)$$

is the flexural rigidity and *Te* represents the effective elastic thickness, a proxy for the depth-integrated strength of the lithosphere (Watts, 2023). We assumed a Young's modulus (E) of 100 GPa, Poisson ratio (ν) of 0.25, gravitational acceleration (g) of 9.81 m s^{-2}, a crustal density (ρ_{load}) of 2700 kg m^{-3}, and a mantle density (ρ_{mantle}) of 3330 kg m^{-3}. We assumed that the material infilling, and displaced by, the flexure was air, such that ρ_{infill} and $\rho_{displace}$ were set to zero. Because *Te* was set to zero at the fault to simulate a plate break and to a uniform finite value for the footwall block, the flexure was computed by solving Eq. (S3) numerically using a finite difference method (Contreras-Reyes and Osses, 2010) for realistic ranges of the two free parameters (*Te* and h_0).

Second, excavation of rock material via glacial erosion causes unloading of the lithosphere and regional flexural uplift (Watts, 2023). We calculated the unload geometry by computing the difference between the observed topography within two deep troughs either side of the Recovery Subglacial Highlands and a horizontal datum close to the 'rims' of the troughs (Fig. S7). Having calculated the unload geometry, we computed the flexure assuming the same set of elastic constants described above. Because erosional unloading is not associated with a plate break, *Te* was set to a uniform finite value, allowing Eq. (S3) to be solved analytically using a fast Fourier transform of the load and convolution with a 1D flexural isostatic response function (Watts, 2023). As was the case for mechanical unloading, we computed the flexure due to erosional unloading for a range of *Te* values.

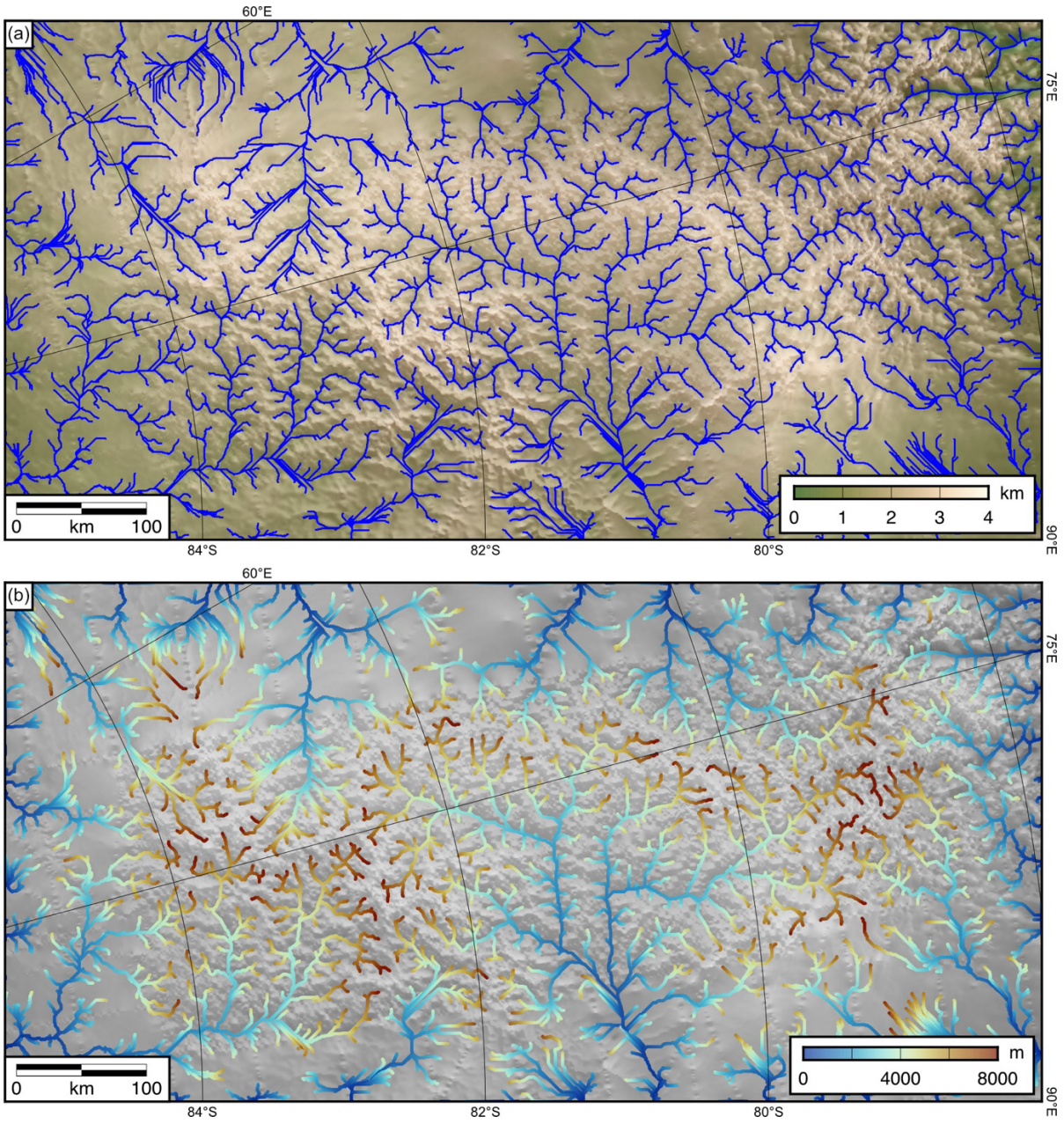

Figure S1: Hydrological flow routing for the Gamburtsevs. (a) Drainage network for an ice-free Gamburtsev landscape, created using TopoToolbox version 3 (Schwanghart and Scherler, 2014). Flow accumulation threshold for stream initiation is 50 km^2. (b) χ map for the Gamburtsevs, computed for $\theta = 0.60$ and $A_0 = 10^6$ m^2. Note that, because the map extent does not reach base level, the absolute values of χ for different drainage basins cannot be compared. However, within a given drainage basin, the relative variation of χ with drainage area will be unaffected by where base level is set.

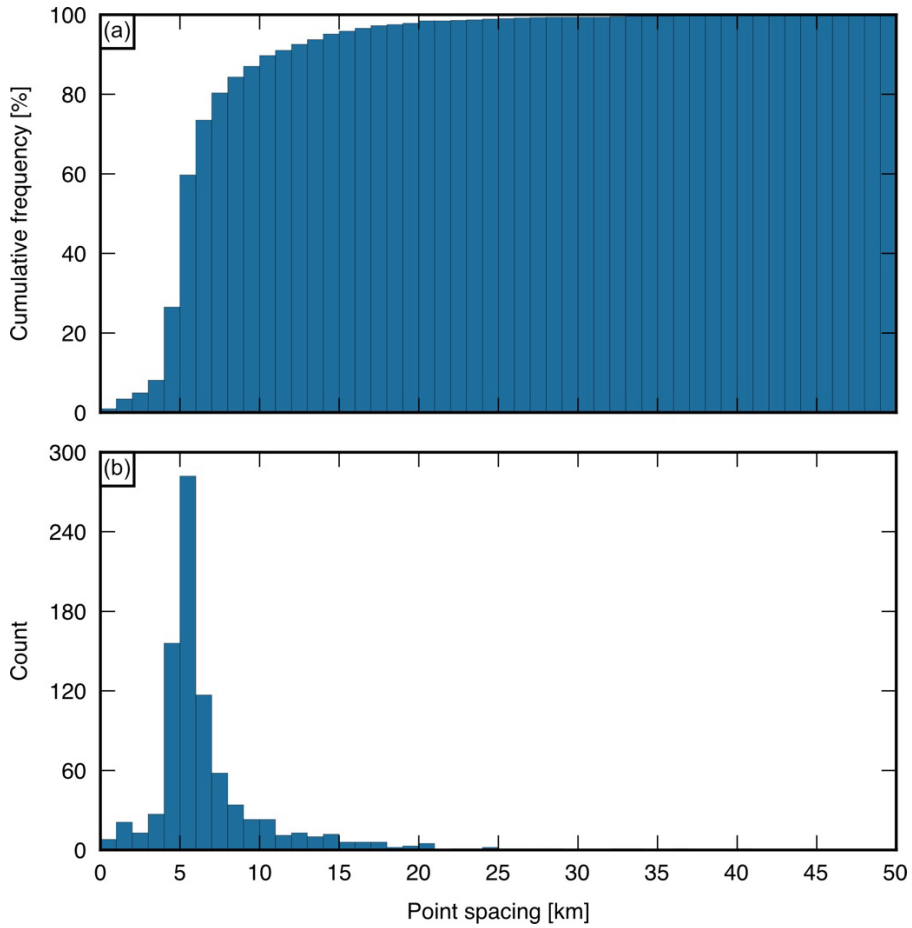

Figure S2: Frequency distribution of the spacing between adjacent RES measurement points along valley thalwegs. (a) Cumulative frequency distribution. (b) Histogram (by count; N = 852). The peak at 5–6 km corresponds to the average AGAP geophysical survey line spacing.

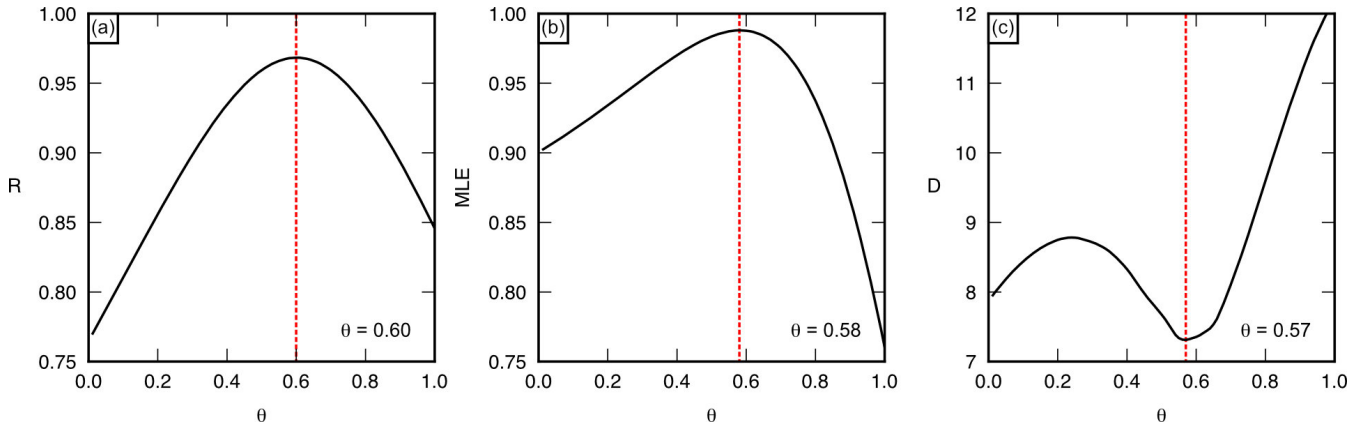

Figure S3: Comparison of methodologies used to identify the most appropriate concavity index (θ) for a drainage basin. (a) Correlation coefficient (R) between χ and elevation for all trunk and tributary nodes, as determined via linear least-squares regression. (b) Maximum likelihood estimator (MLE) calculated from the residuals between the elevation of all tributary nodes and the linear regression of elevation on the trunk valley (i.e., a measure of the degree of collinearity between the tributaries and the trunk valley). (c) The disorder metric (D), a measure of how far tributaries depart from the trunk valley and among themselves in χ-elevation space. Each metric is calculated as a function of θ. Dashed red lines mark the 'best-fit' value of θ for each plot, given by the maximum value of R and MLE, and the minimum value of D.

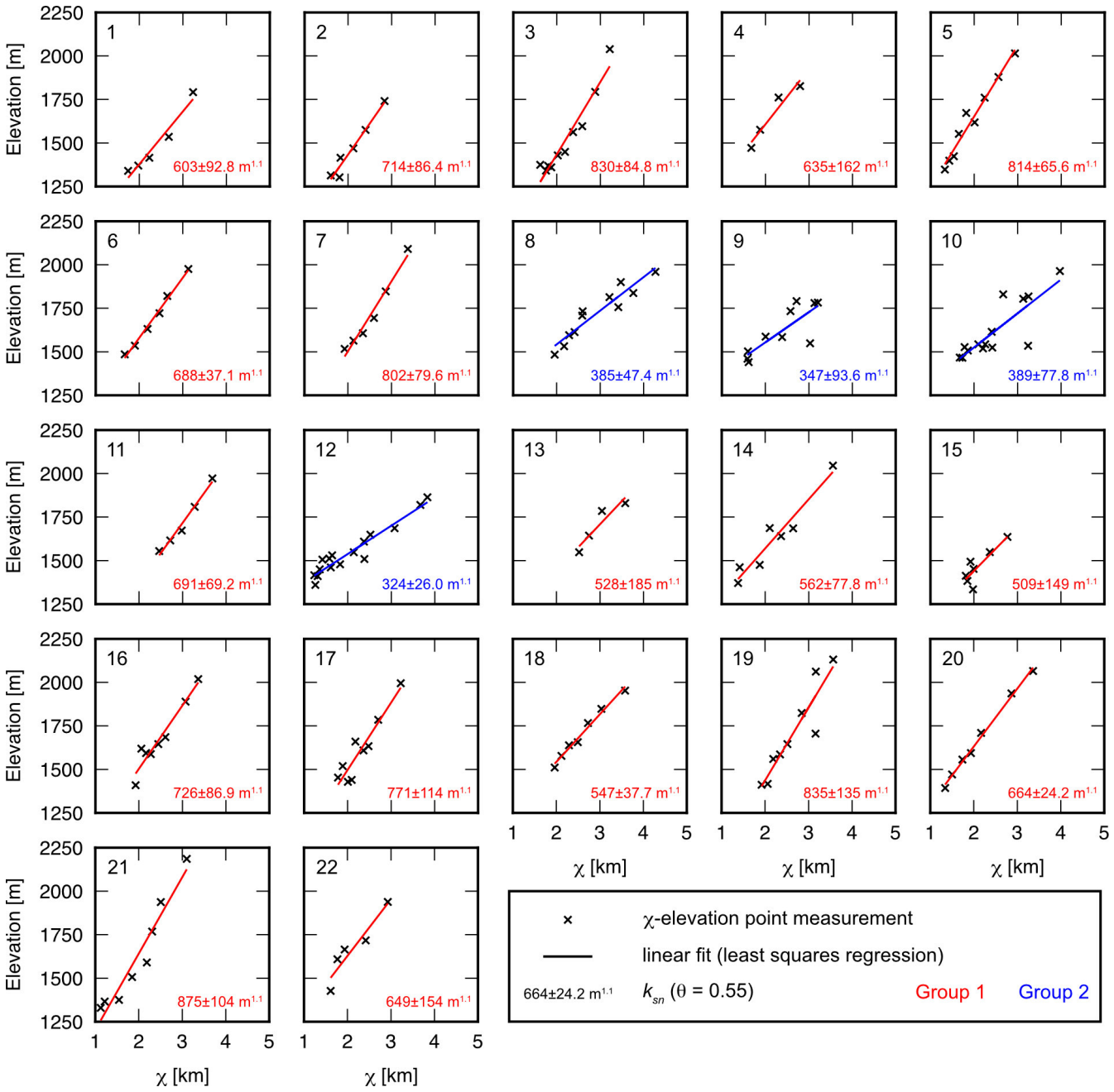

Figure S4: χ analysis and estimation of k_{sn} for valley segments across the northern GSM. χ-elevation plots are constructed for 22 valley segments, each assuming $\theta_{ref} = 0.55$ and $A_0 = 10^6$ m^2. Segment numbers are indicated in the upper left corners of the plots and correspond to the labels in Fig. 6 in the main manuscript. The values of k_{sn} are determined by linear least-squares regression, with uncertainties representing ±1 standard deviation.

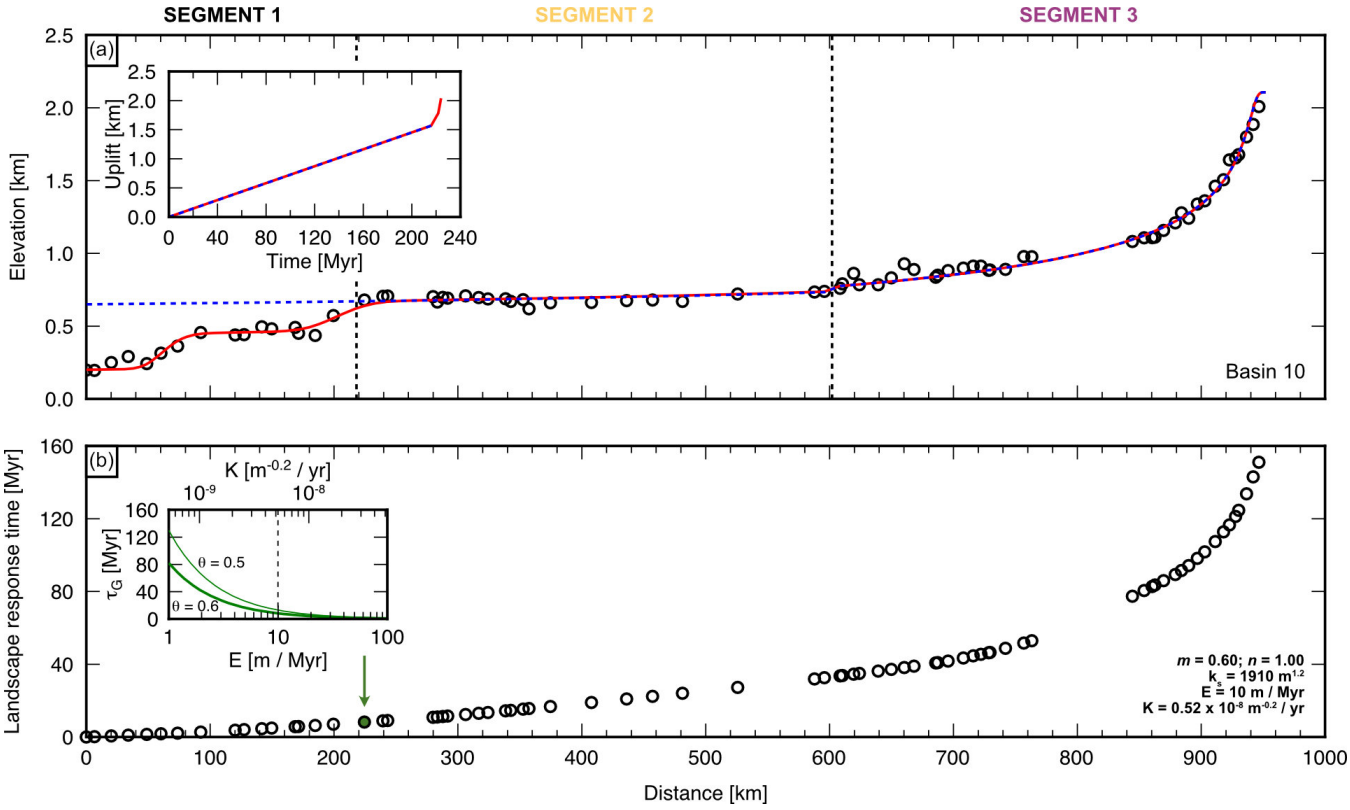

Figure S5: Stream power incision modelling with a temporally variable uplift rate. (a) Comparison between modelled (coloured lines) and observed (circles) longitudinal profiles for basin 10. Vertical dashed lines mark boundaries between profile segments. Dashed blue line is the modelled longitudinal profile with a uniform U (equivalent to Fig. 7a in the main manuscript, except with E decreased to 10 m/Myr and the model run time increased to 216 Myr). The modelled profiles for segments 2 and 3 have been combined, with a step-change in K at the boundary. Red line is a modelled longitudinal profile for a scenario where two pulses of uplift (or base-level fall) are included near the end of the model run. Inset shows the corresponding uplift histories. (b) Landscape response time along the longitudinal profile. Inset shows the landscape response time for the position of the upper knickpoint at ~220 profile-km (green circle and arrow) as a function of E and K. Vertical dashed line marks E = 10 m/Myr. Thick curve is for θ = 0.60; thin curve is for θ = 0.50.

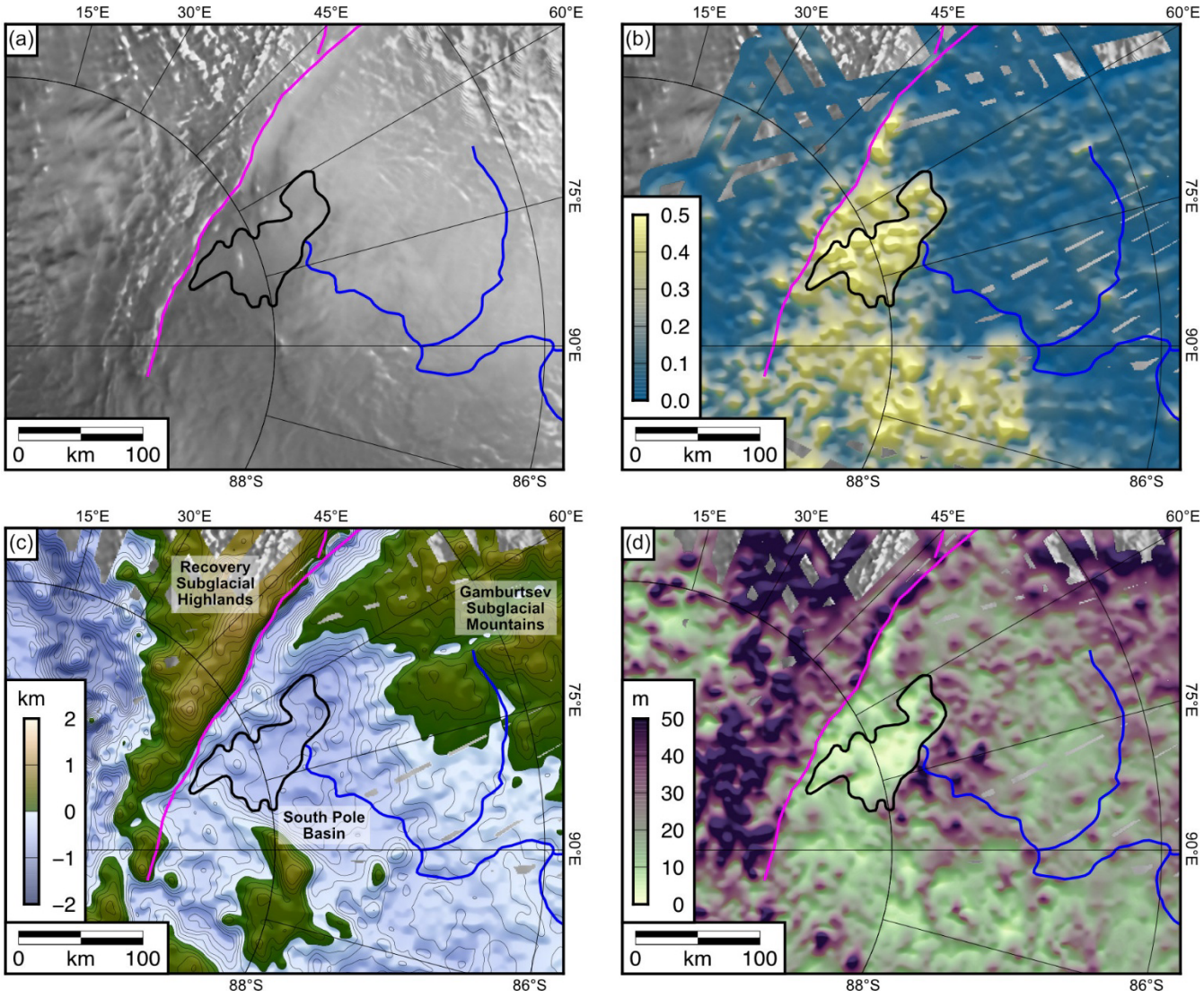

Figure S6: Physiography and basal characteristics of the Recovery Subglacial Highlands and South Pole Basin. (a) RADARSAT RAMP AMM-1 SAR image mosaic version 2 (Jezek et al., 2013). (b) Basal specularity content (Young et al., 2025), (c) bed elevation; contour interval = 100 m (Young et al., 2025), (d) RMS deviation of bed elevation (within a 400 m moving window) (Young et al., 2025). Annotations: purple = linear feature observed in the RAMP AMM-1 SAR image mosaic that coincides with the escarpment separating the elevated, rugged Recovery Subglacial Highlands from the low-lying, smooth South Pole Basin; black = region of smooth bed topography, characterised by and enclosed topographic basin, low RMS deviations of bed elevation (<10 m) and high basal specularity content (>0.4); blue = valley network from Gamburtsev basin 10. Map extent matches Fig. 9b in the main manuscript.

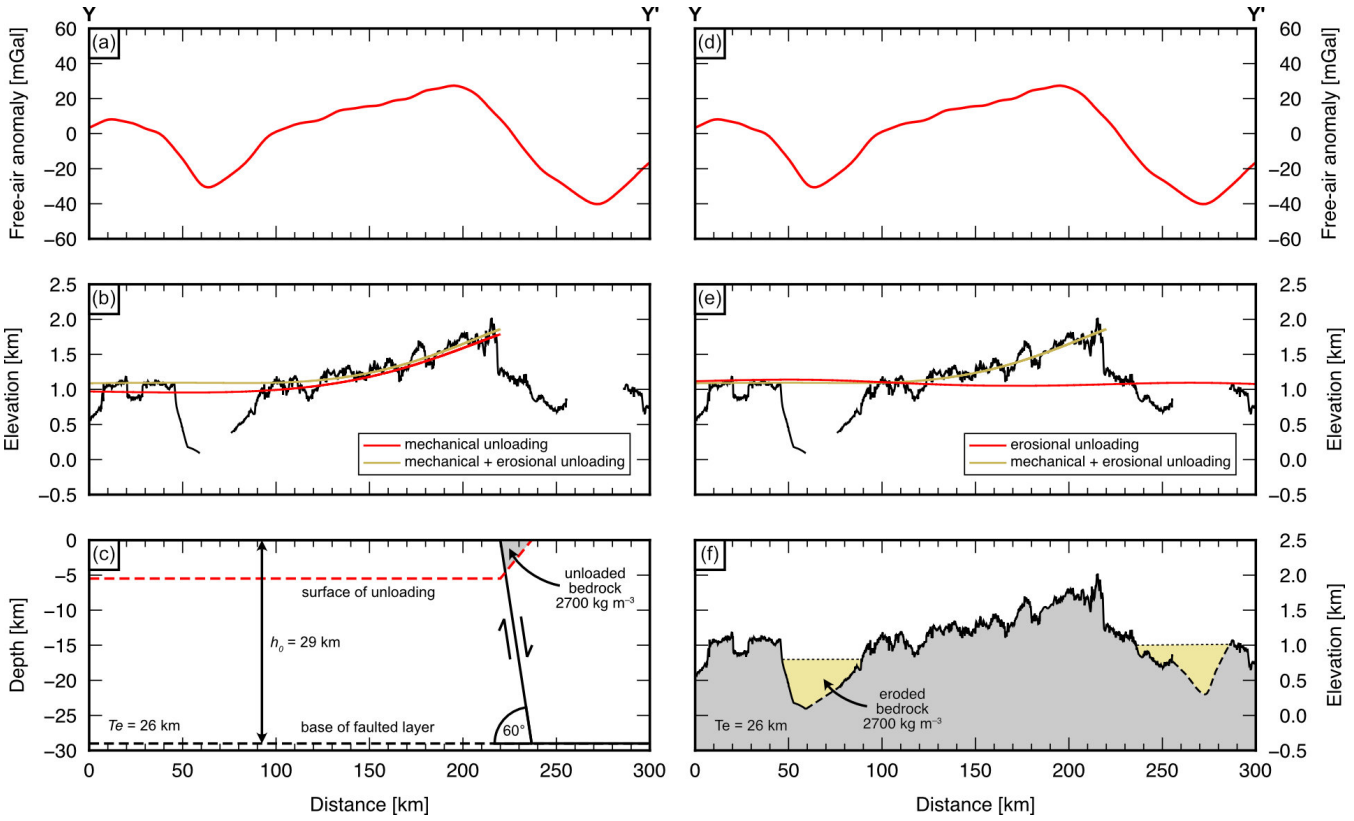

Figure S7: Flexural modelling of Recovery Subglacial Highlands uplift. (a) Free-air gravity anomaly along profile Y–Y' (location shown in Fig. 9 in the main manuscript) (MacGregor et al., 2021). (b) Modelled flexural uplift due to mechanical unloading. Black line is present-day bed elevation isostatically adjusted for the removal of the ice-sheet load (Paxman et al., 2022). Coloured lines show the flexural uplift triggered by mechanical unloading (red) and mechanical and erosional unloading combined (yellow) for a best-fitting combination of Te = 26 km and h_0 = 29 km. (c) Fault model and unloading geometry. We assumed a single, purely normal fault with a typical dip of 60° and a faulted layer thickness of h_0. The grey wedge-shaped region represents the effective unloading experienced by the footwall block due to downward displacement of the hanging-wall block via slip on the fault. The region is bounded by Earth's surface, the fault, and the surface of unloading (elevation of the Moho under isostatic equilibrium in the absence of the crust) (Contreras-Reyes and Osses, 2010; Watts, 2023). (d) Free-air gravity anomaly (same as panel a). (e) As for panel b, except coloured lines show the flexural uplift triggered by erosional unloading (red) and mechanical and erosional unloading combined (yellow). (f) Erosion model and unloading geometry. We assumed erosion was focussed in the broad troughs either side of the highlands. The bed of the trough at ~270 profile-km was not imaged by RES; we used the observed gravity low at this point to approximate the depth of the bed assuming a uniform bedrock density. Troughs were assumed to have been filled to a horizontal datum prior to excavation.

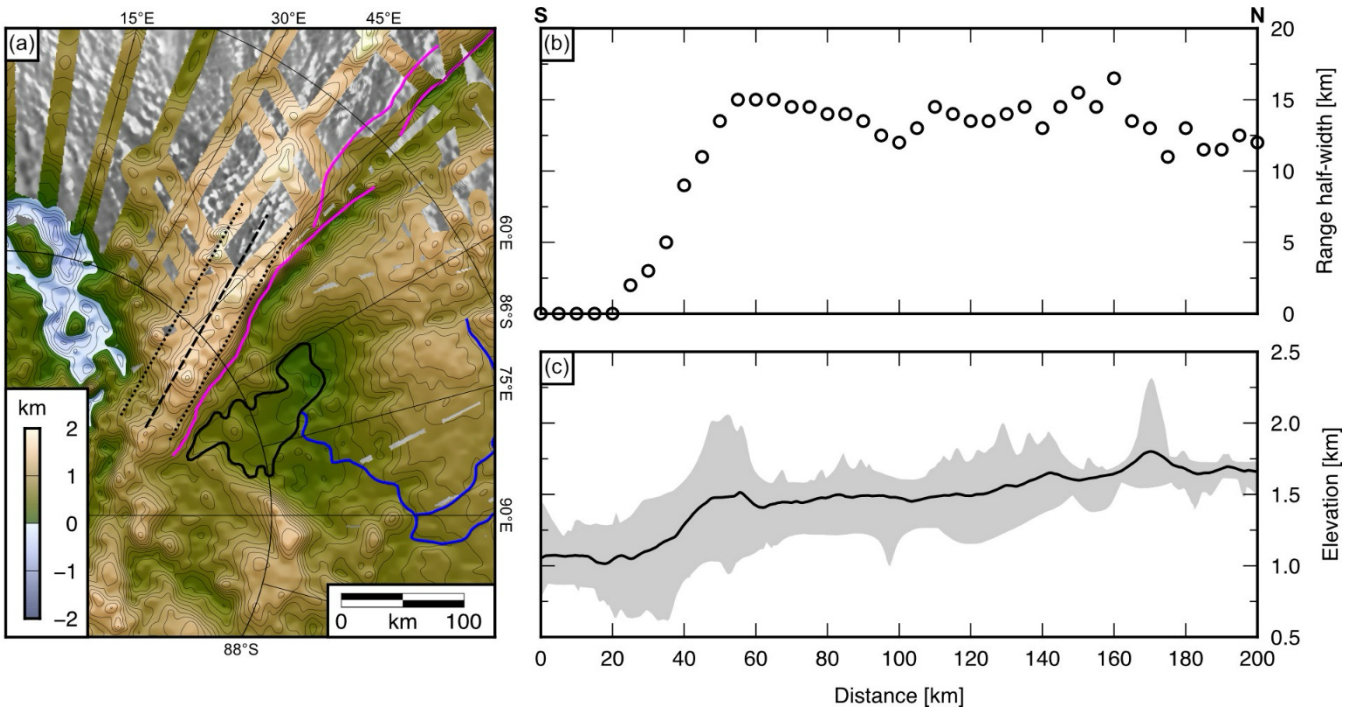

Figure S8: Growth of the Recovery Subglacial Highlands as a normal-faulted range. (a) Rebounded (ice-free) bed topography of the RSH; contour interval = 100 m (Paxman et al., 2022; Young et al., 2025). Annotations: purple = normal-faulted range front; black = smooth basin; blue = valleys. Dashed black lines mark the centre and edges of the topographic swath profile shown in panel c. (b) Range half-width as a function of distance along the RSH range front. Half-width was measured at 5 km intervals along the profile. (c) Swath profile of rebounded bed elevation along the RSH. Solid line marks mean elevation and shaded field indicates the elevation range (minimum to maximum). The swath is oriented south-to-north and constitutes 20 parallel profiles within the region marked in panel a.

Table S1. Longitudinal profile characteristics for the 10 drainage basins mapped in the Gamburtsevs. For basin 10, k_s and k_{sn} values are given for segments (seg.) 2 and 3 (see Fig. 5 in the main manuscript).

Basin	**Number of points**	**Mapped trunk length [km]**	θ **(max. R)**	k_s (θ) $[m^{2\theta}]$	k_{sn} $(\theta_{ref} = 0.55)$ $[m^{1.1}]$
1	39	88.9	-	-	-
2	62	125	0.50	287	776
3	22	54.3	-	-	-
4	37	84.0	-	-	-
5	56	195	0.53	382	573
6	29	87.1	-	-	-
7	43	120	0.55	348	348
8	176	314	0.51	386	861
9	195	297	0.61	2290	650
10	278	947	0.60	seg. 2 = 782; seg. 3 = 1910	seg. 2 = 255; seg. 3 = 667